

Electronic Structure of Chemically-Prepared $\text{Li}_x\text{Mn}_2\text{O}_4$ Determined by Mn X-ray Absorption and Emission Spectroscopies

Craig R. Horne,^{*,†,‡} Uwe Bergmann,[§] Melissa M. Grush,^{||,⊥} Rupert C. C. Perera,[#] David L. Ederer,[±] Thomas A. Callcott,^{||} Elton J. Cairns,^{†,@} and Stephen P. Cramer^{§,∇}

Environmental Energy Technologies Division, Ernest Orlando Lawrence Berkeley National Laboratory, Berkeley, California 94720, Department of Materials Science and Mineral Engineering, University of California, Berkeley, California 94720, Structural Biology Division, Ernest Orlando Lawrence Berkeley National Laboratory, Berkeley, California 94720, Department of Physics and Astronomy, University of Tennessee, Knoxville, Tennessee 37996, Center for X-ray Optics, Ernest Orlando Lawrence Berkeley National Laboratory, Berkeley, California 94720, Tulane University, New Orleans, Louisiana 70118, Department of Chemical Engineering, University of California, Berkeley, California 94720, and Department of Applied Science, University of California, Davis, California 95616

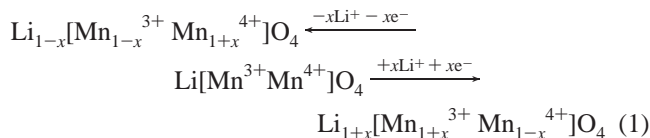
Received: December 23, 1999; In Final Form: July 11, 2000

We have performed Mn K-edge X-ray Absorption and Mn L-edge emission spectroscopies on LiMn_2O_4 , its chemically delithiated and lithiated derivatives ($\lambda\text{-MnO}_2$ and $\text{Li}_2\text{Mn}_2\text{O}_4$, respectively), and two Mn^{3+} spinel model compounds. These experiments were undertaken to understand the associated changes in atomic and electronic structure occurring when LiMn_2O_4 is used in a rechargeable lithium cell. Subtle changes in the Mn K-edge X-ray absorption near edge structure (XANES) occur upon delithiation that are consistent with literature reports of the oxidation of Mn^{3+} to Mn^{4+} , retention of the cubic phase, and contraction of the spinel lattice. Conversely, when LiMn_2O_4 is lithiated, the XANES changes dramatically due to the concurrent transformation from a cubic to a tetragonal spinel. The spectrum is different from XANES of tetragonal Mn^{3+} spinels possessing approximately the same degree of tetragonal distortion as $\text{Li}_2\text{Mn}_2\text{O}_4$. This spectral difference is attributed to the inserted Li^+ imparting an increased degree of covalency within the $\text{Li}_2\text{Mn}_2\text{O}_4$ structure resulting in a $1s \rightarrow 4p + \text{LMCT}$ (ligand to metal charge transfer) shakedown. This increase in covalency was confirmed through Mn L-edge X-ray Emission Spectroscopy measurements. The increased degree of covalency provides insight into the lower Li^+ diffusion coefficients reported in the literature and the electronic conduction mechanism for $\text{Li}_x\text{Mn}_2\text{O}_4$ when $x > 1$.

Introduction

Certain transition-metal oxides possess a high reversible potential versus the lithium electrode resulting in a high specific energy for a Li/metal oxide cell. This property makes transition-metal oxides such as LiCoO_2 , LiNiO_2 , and LiMn_2O_4 desirable as positive electrode materials for rechargeable Li batteries. Among the candidates, LiMn_2O_4 ^{1,2} offers the advantages of low cost and low toxicity over the cobalt or nickel-containing oxides.³ X-ray and neutron diffraction experiments have been the methodology employed in most structural studies of the Li^+ -insertion reaction in LiMn_2O_4 . These studies revealed that upon delithiation of LiMn_2O_4 the lattice contracts while retaining the

cubic structure, whereas lithiating LiMn_2O_4 causes a first-order transformation of the cubic spinel (space group $Fd\bar{3}m$) into the tetragonal phase $\text{Li}_2\text{Mn}_2\text{O}_4$ (space group $I4_1/amd$) with a c/a -axis ratio between 1.16 and 1.18.^{2,4–7} Diffraction methods are sensitive to atomic structure, but the Li^+ -insertion reaction involves changes in electronic as well as atomic structure, according to the proposed reaction:⁴



X-ray absorption near edge structure (XANES) spectra have been utilized in a number of experimental studies on transition-metal oxides to probe the local atomic and electronic structure surrounding the transition metal.^{8–12} XAS studies during delithiation and relithiation of LiMn_2O_4 were reported by Ammundsen et al. for chemically prepared samples^{13,14} and Shiraishi et al.¹⁵ along with Shinshu et al.¹⁶ for electrochemically prepared samples. Their findings supported the left-half of the proposed insertion reaction mechanism (1) and showed that delithiation is not accompanied by a large change in local structure. Additionally, it has been shown that the L-edge X-ray emission spectroscopy (L-XES) of transition metals is sensitive to the degree of covalency through the L_α/L_β emission ratio.

* Corresponding author. Present address: NanoGram Corp., Fremont, CA 94538.

† Environmental Energy Technologies Division, Ernest Orlando Lawrence Berkeley National Laboratory.

‡ Department of Materials Science and Mineral Engineering, University of California, Berkeley.

§ Structural Biology Division, Ernest Orlando Lawrence Berkeley National Laboratory.

|| University of Tennessee.

⊥ Present address: Stanford Synchrotron Radiation Laboratory, Menlo Park, CA 9430.

Center for X-ray Optics, Ernest Orlando Lawrence Berkeley National Laboratory.

± Tulane University.

@ Department of Chemical Engineering, University of California, Berkeley.

∇ Department of Applied Science, University of California, Davis.

This was originally shown for Cu compounds¹⁷ and has been more recently demonstrated with Mn compounds¹⁸ and applied to substituted LiMn_2O_4 materials.¹⁹

Both XANES and L-XES spectroscopies provide a method to obtain electronic structural information with a sample in the functional form (the powder within a Li rechargeable battery composite electrode) and at the service temperature (room temperature) of the material. In contrast, determining electronic structure through property measurements such as magnetic susceptibility, electrical conductivity, and/or Seebeck coefficient involves collecting data at high and low temperatures and, in the case of the latter two techniques, processing the powder into a monolithic shape which may not be representative of the powder.²⁰ Furthermore, the low decomposition temperature of delithiated and lithiated LiMn_2O_4 ^{21,22} limits the temperature range for synthesis of the necessary monoliths. Also, XANES and L-XES are bulk probes of the structure and thus not highly sensitive to surface defects. In the case of LiMn_2O_4 , the penetration depth of an X-ray photon at the Mn K-edge is on the order of the particle size, 9 μm , and that of Mn L_{α} photons are approximately 0.25 μm . In contrast, X-ray photoelectron spectroscopy is much more surface sensitive with a penetration depth of approximately 20 Å;²³ this dimension is on the order of two spinel unit cells.

In light of these considerations and the aforementioned role of electronic structure in this system, we have performed XANES and L-XES measurements on LiMn_2O_4 along with its lithiated derivative, delithiated derivative, and two Mn^{3+} spinel model compounds. This effort was undertaken in order to understand the changes occurring in the local electronic and atomic structure of LiMn_2O_4 as a function of lithium content. We have applied XANES and L-XES to the fully lithiated material where the electronic structure is markedly different from that expected based upon the local atomic structure. By evaluating the local atomic and electronic structural changes occurring upon both delithiation and lithiation we have obtained an improved insight into the Li insertion-reaction mechanism. Additionally, our findings show the importance of directly determining the local electronic structure in oxides such as $\text{Li}_x\text{Mn}_2\text{O}_4$ (where x represents lithium contents between 0.1 and 2.0) using techniques such as XANES and L-XES. This methodology is in contrast to the more common approach of inferring the electronic structure based upon the local atomic structure derived from refinements of diffraction data.

Experimental Apparatus and Procedures

One LiMn_2O_4 powder used in this work, denoted $\text{LiMn}_2\text{O}_4\text{-A}$, was a gift from Chemetal, Inc. Lithium extraction to yield $\lambda\text{-MnO}_2$ was performed using the procedure of Hunter:²¹ 3 g of spinel were added to 80 mL of 1 M H_2SO_4 , stirred in an open container for 26 h and then dried overnight at 85 °C under a vacuum of 25 in. Hg. Lithium insertion was accomplished using the method of Tarascon et al.²⁴ Two grams of spinel were placed in 75 mL of a 1.33 M solution of LiI in CH_3CN and refluxed under an Ar atmosphere for 4.5 h. Afterward, the solution was filtered, rinsed thoroughly in clean CH_3CN , and dried overnight at 85 °C under a vacuum of 25 in. Hg. This lithiated powder is denoted $\text{Li}_2\text{Mn}_2\text{O}_4\text{-A}$.

The other LiMn_2O_4 powder used in this work, denoted as $\text{LiMn}_2\text{O}_4\text{-B}$, was synthesized in our laboratory. MnO_2 (CMD, IC#5 from Japan Metals and Chemical) and $\text{LiOH}\cdot\text{H}_2\text{O}$ (Spectrum Chemical, 99.9% purity) were mixed in *n*-hexane and then heated at 20 °C/min to 750 °C for 40 h with furnace cooling. The powder was then reground in *n*-hexane, reheated at 20 °C/

min to 750 °C for 40 h, cooled at 0.8 °C/min to 100 °C, and finally reground in *n*-hexane. Chemical lithiation as described above was performed on a portion of this powder and is denoted as $\text{Li}_2\text{Mn}_2\text{O}_4\text{-B}$.

The tetragonal spinels ZnMn_2O_4 and MgMn_2O_4 were synthesized by mixing stoichiometric amounts of $3\text{Zn}(\text{OH})_2\cdot 2\text{Zn}(\text{CO}_3)$ (from EM Science GR) or $4\text{Mg}(\text{CO}_3)\cdot\text{Mg}(\text{OH})_2\cdot 4\text{H}_2\text{O}$ (Mallicnrodt AR) with MnCO_3 (Baker Reagent) and acetone in a ball-mill for 3 h, using 2 mm diameter yttria-stabilized zirconia balls. After mixing, the powders were fired first at 900 °C for 24 h and then at 1050 °C for 48 h. A 0.8 °C/min cooling rate was used in both firing steps, and the powders were ground in *n*-hexane after each firing.

X-ray diffraction (XRD) was performed with a Siemens D5000 diffractometer using Cu K α radiation and a diffracted beam graphite monochromator. Data were collected over a range of 15 to 90° 2 θ using a 0.05° step size and a 2 s counting time. A 2 θ calibration function was generated by fitting a second-order polynomial to the shift in the Si peak position on the 2 θ scale. The shifts of the Si peak positions were determined by the difference between the observed peak positions of an internal Si standard and those calculated based upon a lattice parameter of 5.4309 Å. Lattice parameters of the spinels were obtained by refining the calibrated 2 θ peak positions using a nonlinear least squares algorithm found in the program *UnitCell* '96²⁵ to minimize the residuals in 2 θ .

The lattice parameter of the Chemetal LiMn_2O_4 ($\text{LiMn}_2\text{O}_4\text{-A}$) was found to be 8.245 Å. The synthesized $\lambda\text{-MnO}_2$ was determined by XRD to possess a lattice parameter of 8.043 Å; consistent with the reported formula $\text{Li}_{0.2}\text{Mn}_2\text{O}_4$.^{7,26,27} The XRD pattern of $\text{Li}_2\text{Mn}_2\text{O}_4\text{-A}$ showed that full conversion to a tetragonal spinel was achieved. The resulting lattice parameters were $a_t = 5.654$ Å and $c_t = 9.249$ Å; these dimensions are similar to those previously reported for the formula $\text{Li}_{2.0}\text{Mn}_2\text{O}_4$ in refs 5 through 7. The lattice parameter of $\text{LiMn}_2\text{O}_4\text{-B}$ was found to be 8.231 Å whereas those of $\text{Li}_2\text{Mn}_2\text{O}_4\text{-B}$ were $a_t = 5.655$ Å and $c_t = 9.187$ Å. The unit cell volumes between the two sets of LiMn_2O_4 and $\text{Li}_2\text{Mn}_2\text{O}_4$ compounds differ by less than 0.5%. The lattice parameters of ZnMn_2O_4 were $a_t = 5.715$ Å and $c_t = 9.256$ Å; those of MgMn_2O_4 were $a_t = 5.726$ Å and $c_t = 9.333$ Å. These values are consistent with those reported in refs 28 and 29, respectively. No peaks attributable to impurity phases were found within the XRD patterns from the materials used in this study.

Manganese K-edge XANES were collected at the Stanford Synchrotron Radiation Laboratory (SSRL) on bend magnet Beamline 2–3 with a Si(220) double-crystal monochromator and 0.5 mm vertical, 2 mm horizontal exit slits. To reduce the amount of higher harmonics, the incident beam was detuned to 33% of the maximum intensity. The ring energy was 3.0 GeV with 100 mA current at the top of the fill. Data were collected with a 0.25 eV step size and a 2 s counting time through the edge region. Data reduction was performed using the EXAF-SPAK analysis package available from SSRL. Transmission data from two scans of each sample were averaged and the background was subtracted using a straight line from 6310 to 6520 eV. The XANES were normalized at 6575 eV to a quartic spline fit through the atomic falloff. Second derivatives were calculated after smoothing with a third-order polynomial over a 1.5 eV window. For the XANES measurements, oxide powders were mixed in a 1:16 ratio with boron nitride (BN) using a mortar and pestle. After mixing, 0.150 g was placed in a 0.17 cm thick sample holder (1.3 cm diameter) and enclosed with 0.002 in. thick Kapton tape. Preparation of the air-sensitive

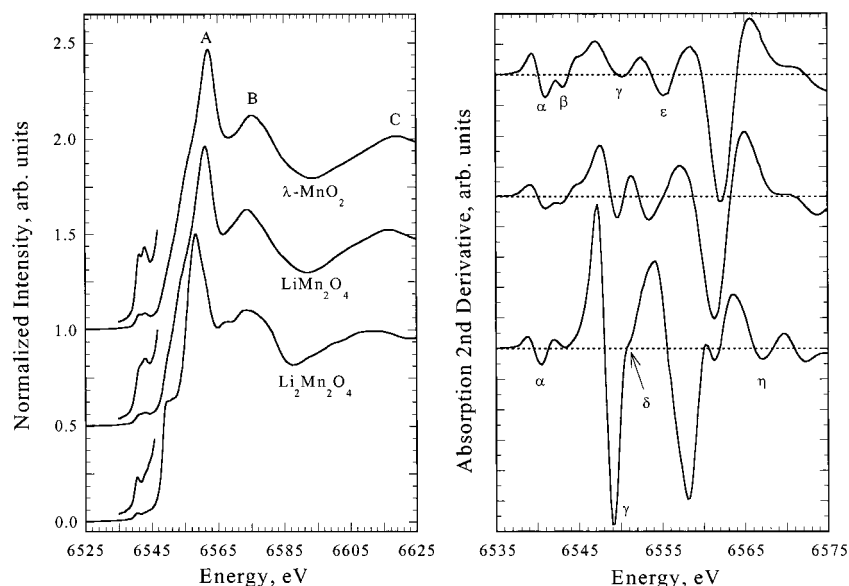


Figure 1. (Left) normalized XANES of $\text{LiMn}_2\text{O}_4\text{-A}$ along with chemically prepared $\lambda\text{-MnO}_2$ and $\text{Li}_2\text{Mn}_2\text{O}_4\text{-A}$. Inset shows magnified view of the preedge. (Right) second derivative of each XANES. Note that features α , β , γ , ϵ , and η correspond to local minima whereas feature δ corresponds to the point where the derivative value is zero.

TABLE 1: XANES Peak Positions for Spectra Shown in Figures 1–3^a

sample	energy position, eV								
	α	β	γ	δ	ϵ	A	η	B	C
$\lambda\text{-MnO}_2$	6541.1	6543.2	6550.3		6555.4	6562.1		6575.4	6619.5
$\text{LiMn}_2\text{O}_4\text{-A}$	6541.1	6542.9	6549.6		6553.5	6561.1		6573.9	6616.5
$\text{Li}_2\text{Mn}_2\text{O}_4\text{-A}$	6540.6		6549.1	6550.8		6558.3	6567.0	6573.6	6613.5
$\text{LiMn}_2\text{O}_4\text{-B}$	6541.0	6543.0	6549.8		6553.7	6561.2		6574.0	6616.4
$\text{Li}_2\text{Mn}_2\text{O}_4\text{-B}$	6540.4		6549.1	6550.8		6558.4	6567.1	6573.4	6612.3
MgMn_2O_4	6540.4		6551.2	6553.1		6559.6		6572.2	6611.6
ZnMn_2O_4	6540.4		6551.7	6553.3		6560.0		6572.0	6612.4

^a The notation A corresponds to LiMn_2O_4 and $\text{Li}_2\text{Mn}_2\text{O}_4$ originating from Chemetal LiMn_2O_4 whereas B denotes those originating from LiMn_2O_4 synthesized in our laboratory. Positions of features denoted by Roman letters correspond to features in the XANES spectrum while those denoted by Greek letters were determined from the second derivatives.

$\text{Li}_2\text{Mn}_2\text{O}_4$ XAS sample was performed in an Ar-filled glovebag using anhydrous BN. The thickness of each sample was determined to be approximately one absorption length at the Mn K-edge.

Manganese L-XES spectra were recorded using the University of Tennessee soft X-ray fluorescence endstation on Beamline 8.0 at the Advanced Light Source. This is an undulator beamline with a spherical grating monochromator, as has been previously described.³⁰ The ring energy was 1.9 GeV and the current at the top of the fill was 400 mA. A 925 l/mm grating was used to monochromatize the above threshold excitation energy for Mn at ~ 680 eV. The soft X-ray fluorescence endstation³⁰ consists of a Rowland circle-type emission spectrometer with a fixed entrance slit and a 1500 l/mm grating mounted on a 10 m Rowland circle. The X-ray fluorescence is refocused onto a multichannel plate area detector, enabling the entire emission spectrum to be obtained without scanning the detector. With an entrance slit of 50 μm , the resolution of this detector corresponds to approximately 1.1 eV in the Mn fluorescence region. Data collection was ~ 20 min and the resultant spectra were then smoothed over a 13 point region using the commercially available program *Origin*. Mn Emission spectra were set to zero intensity at 680 eV, normalized to unit intensity at the L_β peak, and calibrated relative to the L_β emission of MnO .³¹ For the L-XES measurements, the pure oxide powders were pressed into pellets. The $\text{Li}_2\text{Mn}_2\text{O}_4$ sample ($\text{Li}_2\text{Mn}_2\text{O}_4\text{-B}$) was prepared in a N_2 glovebag. All L-XES samples were measured in a vacuum of better than 1×10^{-8} Torr.

Results

Mn K-edge XANES of $\text{LiMn}_2\text{O}_4\text{-A}$ and chemically prepared $\lambda\text{-MnO}_2$ and $\text{Li}_2\text{Mn}_2\text{O}_4\text{-A}$ are given in Figure 1(left); a magnification of the preedge region is included to facilitate comparison. The XANES second derivatives are shown in the right panel of Figure 1. The energy positions of the spectral features labeled in Figure 1 are shown in Table 1 using the convention of capital Roman letters (A, B, C) to denote XANES features and small Greek letters (α , β , γ , δ , ϵ , η) to denote XANES second derivative features. The spectral shapes from the chemically prepared samples are consistent with spectra measured on electrochemically delithiated and lithiated samples.³² Consequently, further discussion concerning the tetragonal spinel $\text{Li}_2\text{Mn}_2\text{O}_4$ is applicable to the entire range of tetragonal compositions, $1.8 \leq x \leq 2.2$,⁷ and we invoke the general term $t\text{-Li}_x\text{Mn}_2\text{O}_4$ interchangeably with $\text{Li}_2\text{Mn}_2\text{O}_4$ for structural interpretation. In a similar manner the term $c\text{-Li}_x\text{Mn}_2\text{O}_4$ will be applied to the entire range of cubic compositions, $0.1 \leq x \leq 1.0$.⁷ However, $\lambda\text{-MnO}_2$ and $\text{Li}_2\text{Mn}_2\text{O}_4$ will be used when referring specifically to the XANES measured in this study. These assignments are important for correlating the structural observations to the electrochemical properties and performance later in this paper.

A first observation from Figure 1 and the data in Table 1 is that the spectral features shift in energy upon changing the Li content. The shifts to higher energy upon delithiation and lower energy upon lithiation (as compared to the position of $\text{LiMn}_2\text{O}_4\text{-A}$

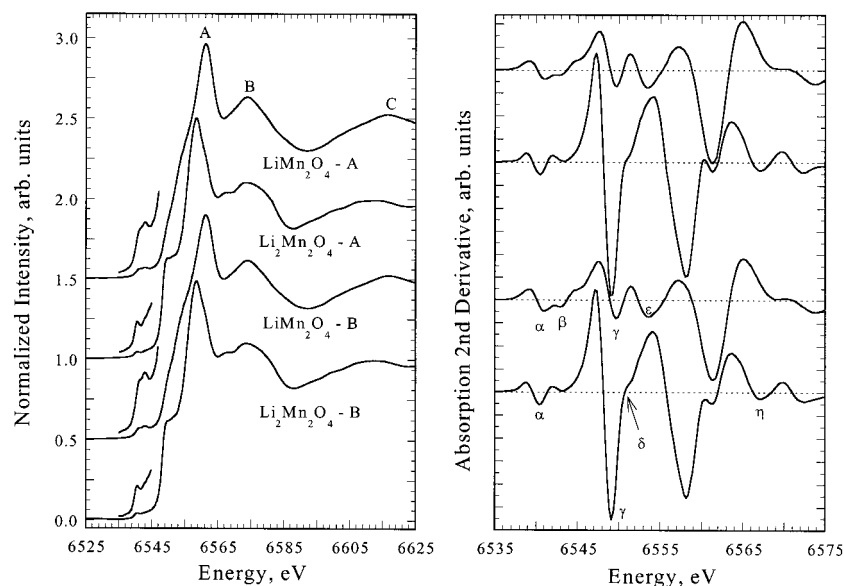


Figure 2. (Left) normalized XANES of LiMn_2O_4 from two different sources and corresponding $\text{Li}_2\text{Mn}_2\text{O}_4$ synthesized from each. Inset shows magnified view of the preedge region. (Right) second derivative of each XANES as described in Figure 1.

A) suggest that the average Mn oxidation state changes according to reaction 1. However, the magnitudes of the shifts from $\text{LiMn}_2\text{O}_4\text{-A}$ are different; approximately +1 eV upon delithiation (i.e., oxidizing the $[\text{Mn}^{3+}\text{O}_6]$ octahedra) versus -2.8 eV when lithiating (i.e., reducing the $[\text{Mn}^{4+}\text{O}_6]$ octahedra). This difference in the magnitude of the edge shift upon delithiation and lithiation will be discussed below.

Differences in the spectral shapes of the preedge and main edge upon changing the lithium content are apparent upon inspecting both the XANES (Figure 1, left) and the second derivative XANES (Figure 1, right). Changes occurring upon delithiation are relatively minor. Small differences are seen in the preedge region, however, the rising edge and above threshold regions are very similar in the $\text{LiMn}_2\text{O}_4\text{-A}$ and $\lambda\text{-MnO}_2$ spectra. These observations are consistent with the XANES data presented in refs 13–15 and 32. The similarity between the $\text{LiMn}_2\text{O}_4\text{-A}$ and $\lambda\text{-MnO}_2$ spectra is not surprising since there is a change only in unit cell dimensions and not in crystal structure upon delithiation. Conversely, there is a large alteration of the spectral shape upon lithiation. The most significant change is the manifestation of a step halfway up the edge. This type of feature has been associated with square-planar transition-metal compounds^{33–36} and with a $1s \rightarrow 4p + \text{LMCT}$ shakedown process in copper compounds;^{37–39} further discussion of this topic is found below. Lithiation also results in an additional peak forming (feature η) approximately 8 eV above the main peak as noted in Table 1. This additional peak was also found in both the Cr and Mn XANES of lithiated, Cr-substituted spinels, $\text{Li}_2\text{Mn}_{2-y}\text{Cr}_y\text{O}_4$ ($y = 0.2$ and 1.0).⁴⁰ In general, higher energy XANES peaks have been attributed to multiple scattering from surrounding shells^{9,11,13} as discussed below. Both the manifestation of a step in the edge and the peak associated with feature η were also found in both the Cr and Mn XANES of lithiated, Cr-substituted spinels, $\text{Li}_2\text{Mn}_{2-y}\text{Cr}_y\text{O}_4$ ($y = 0.2$ and 1.0).⁴⁰

The qualitative similarity between the XANES from square-planar compounds and the $\text{Li}_2\text{Mn}_2\text{O}_4\text{-A}$ XANES, as indicated by the presence of a step halfway up the edge, is surprising since the Mn site in $\text{t-Li}_x\text{Mn}_2\text{O}_4$ is within a tetragonally distorted $[\text{MnO}_6]$ octahedron possessing a c/a -axis ratio between 1.16 and 1.18.^{2,5–7} To ascertain if this result was dependent on the source of the LiMn_2O_4 material we also measured the XANES

of $\text{LiMn}_2\text{O}_4\text{-B}$ synthesized in our laboratory, along with the chemically lithiated derivative of this powder, $\text{Li}_2\text{Mn}_2\text{O}_4\text{-B}$. There is excellent agreement between the XANES of these two sets of materials as shown by the data in Figure 2 and Table 1. As mentioned at the beginning of this section, the XANES and the second derivative spectral features of both chemically lithiated powders are in good agreement with the XANES of electrochemically lithiated samples of $\text{t-Li}_x\text{Mn}_2\text{O}_4$.³² This indicates that the edge step manifests from local atomic and electronic structural characteristics of $\text{t-Li}_x\text{Mn}_2\text{O}_4$ rather than being specific to one sample or an artifact due to the method of preparation. Given the similarities of the two $\text{Li}_2\text{Mn}_2\text{O}_4$ spectra further discussion will not be specific to sample origin.

To assist in understanding the $\text{t-Li}_x\text{Mn}_2\text{O}_4$ structure we measured the XANES of two model tetragonal Mn^{3+} spinels, ZnMn_2O_4 and MgMn_2O_4 . The atomic structures of these oxides are very similar to $\text{Li}_2\text{Mn}_2\text{O}_4$; both belong to space group $I4_1/amd$ with c/a -axis ratios equal to 1.14.^{28,29} The Zn or Mg ions reside in a tetrahedral site, whereas the Mn occupy an octahedral site. Figure 3 compares the spectra of the model compounds with that of $\text{Li}_2\text{Mn}_2\text{O}_4$; the second derivatives of the XANES are shown in the right panel of Figure 3. The preedges of these compounds are relatively similar while the edges differ in several aspects. A shoulder instead of a step is observed in the rising edge of the model compound XANES. Table 2 shows that the energy separations between the main peak (A) and the shoulder in the edge (δ) are approximately 1 eV lower in the model compounds as compared to $\text{Li}_2\text{Mn}_2\text{O}_4$. Additionally, the main peak (A) and edge shoulder/edge step energies (δ) are shifted approximately 1 and 2 eV, respectively, to higher energy in the model compounds as compared to $\text{Li}_2\text{Mn}_2\text{O}_4$. Last, the structure of peak (B) differs; the additional $\text{Li}_2\text{Mn}_2\text{O}_4$ XANES feature at approximately 6568 eV, not found in the parent LiMn_2O_4 XANES, is also not present in the model compound XANES.

The fact that the XANES main peak (A) is at a lower energy for $\text{Li}_2\text{Mn}_2\text{O}_4$ compared to the model compounds suggests that a greater degree of covalency may exist within the former compound for reasons discussed in the next section. To ascertain whether this assertion is correct, we have measured the Mn L-XES to compare the relative degree of covalency between these three compounds.

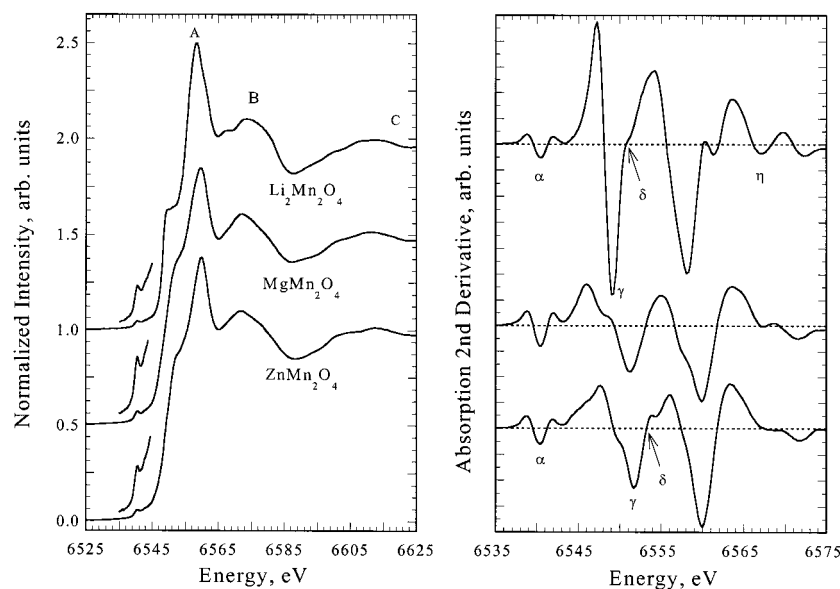


Figure 3. (Left) comparison of XANES from $\text{Li}_2\text{Mn}_2\text{O}_4$ with the tetragonal spinels ZnMn_2O_4 and MgMn_2O_4 . (Right) second derivative of each XANES as described in Figure 1.

TABLE 2: Energy Difference between Features A and δ in XANES of $\text{Li}_2\text{Mn}_2\text{O}_4$, MgMn_2O_4 , and ZnMn_2O_4 and As Compared to $\text{Li}_2\text{Mn}_2\text{O}_4$

	$\text{Li}_2\text{Mn}_2\text{O}_4\text{-A}$	$\text{Li}_2\text{Mn}_2\text{O}_4\text{-B}$	MgMn_2O_4	ZnMn_2O_4
$\Delta E_{A-\delta}$	7.5	7.6	6.5	6.7
$\Delta\delta$ (vs $\text{Li}_2\text{Mn}_2\text{O}_4$)			+2.3	+2.5

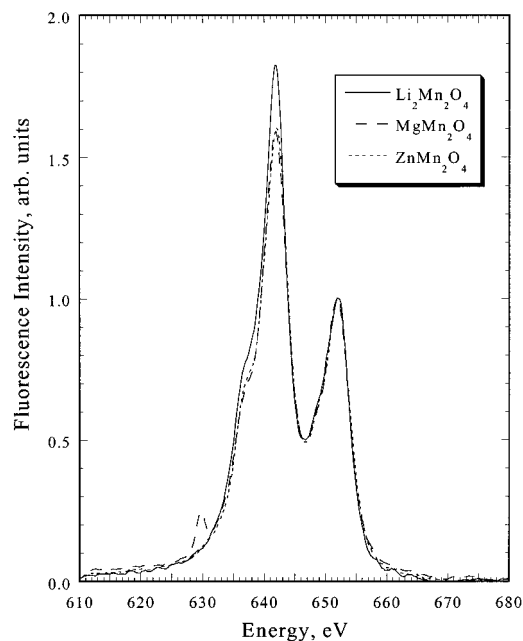


Figure 4. Manganese L-edge XES spectra for $\text{Li}_2\text{Mn}_2\text{O}_4$ (solid line), MgMn_2O_4 (dash-dotted line), and ZnMn_2O_4 (dashed line).

The L-emission spectra of $\text{Li}_2\text{Mn}_2\text{O}_4$ and the model Mn^{3+} tetragonal spinels are shown in Figure 4. All three spectra exhibit similar structure: two main peaks (L_α and L_β) with lower energy shoulders occurring at the same energy. The small peak at ~ 629.5 eV in the spectrum of MgMn_2O_4 is due to Mg $K\alpha$ emission recorded in 2nd order. This transition is made possible due to higher order reflections of the incident X-ray photons. The integrated peak ratios, determined by simulating the spectra with a series of four Lorentzians, are shown in Table 3. Figure 5 compares the fitted and experimental $\text{Li}_2\text{Mn}_2\text{O}_4$ L-emission spectra and also shows the four constituent peaks of the

TABLE 3: Mn L-Edge XES Integrated Peak Ratios for $\text{Li}_2\text{Mn}_2\text{O}_4$, MgMn_2O_4 , and ZnMn_2O_4

sample	peak no.	peak area
$\text{Li}_2\text{Mn}_2\text{O}_4$	1	3.04
	2	9.07
	3	0.02
	4	3.32
	L_α/L_β ratio	3.63
MgMn_2O_4	1	3.47
	2	10.7
	3	1.71
	4	4.87
	L_α/L_β ratio	2.15
ZnMn_2O_4	1	3.25
	2	11.0
	3	2.14
	4	4.37
	L_α/L_β ratio	2.18
	L_α/L_β ratio = (1 + 2)/(3 + 4)	

simulation. The Mn L_α and L_β regions of the spectra are almost identical for ZnMn_2O_4 and MgMn_2O_4 whereas $\text{Li}_2\text{Mn}_2\text{O}_4$ has higher integrated intensity in the L_α region, with respect to the L_β region where the spectra were normalized. The L_α/L_β ratios for ZnMn_2O_4 and MgMn_2O_4 are 2.15 and 2.18, respectively, and the ratio for $\text{Li}_2\text{Mn}_2\text{O}_4$ is 3.63. A larger L_α/L_β ratio corresponds to a higher degree of covalency^{19,31} and thus the simulation results substantiate the assertion that the degree of covalency is greater in the lithiated Mn^{3+} spinel as compared to the model Mn^{3+} tetragonal spinels.

Discussion

XANES Preedge Structure. The preedge absorption features in the XANES are assigned to a $1s \rightarrow 3d$ transition. Though this transition is dipole-forbidden for centrosymmetric compounds due to parity considerations, weak preedge features are commonly observed in the XANES of such compounds. Preedge transitions in the XANES of a centrosymmetric CuCl_4^{2-} single crystal were shown to originate primarily from coupling to the electric quadrupolar component of the radiation.⁴¹ A smaller contribution (approximately one-quarter of the total value) was attributed to a vibronically allowed dipole coupling mechanism

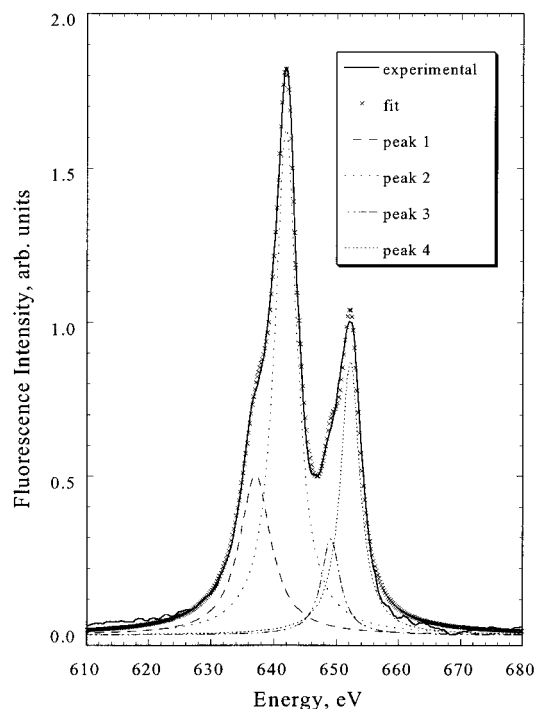


Figure 5. Comparison of fitted and experimental $\text{Li}_2\text{Mn}_2\text{O}_4$ L-emission spectra. Also shown are the four constituent peaks of the simulation.

as the CuCl_4^{2-} compound possessed a center of inversion. The Mn site in $c\text{-Li}_x\text{Mn}_2\text{O}_4$, 16d within the space group $Fd\bar{3}m$, possesses a center of inversion whereas the Mn site in $t\text{-Li}_x\text{Mn}_2\text{O}_4$, 8d within the space group $I4_1/amd$, does not.⁴² Furthermore, Fourier Transform Infrared spectroscopy studies have shown that the vibrational spectra of spinels are sensitive to the A-site occupancy.⁴³ Therefore, it would be expected that the vibrational-based contribution to the preedge peak intensity will differ among the compounds studied here which, in turn, would affect a comparison similar to that performed in ref 12.

LiMn_2O_4 is a type II mixed-valent compound containing a 1:1 mixture of Mn^{3+} and Mn^{4+} to give $\bar{z}_{\text{Mn}} = +3.50$. Reports that LiMn_2O_4 is a small polaron conductor⁴⁴ and the measured effective magnetic moment⁴⁵ are consistent with this interpretation of Mn oxidation state versus one in which each Mn possess an oxidation state of +3.5.⁴⁶ The mixture of oxidation states leads to a mixture of $1s \rightarrow 3d$ transition energies and consequently broadens the preedge spectra. Chemical delithiation to $\text{Li}_{0.1}\text{Mn}_2\text{O}_4$ oxidizes the Mn^{3+} , resulting in a 90% Mn^{4+} compound. This explains the sharpening observed in the preedge of $\lambda\text{-MnO}_2$ versus the parent LiMn_2O_4 (see Figure 1, left) along with the increased preedge peak energy of $\lambda\text{-MnO}_2$ (features (α) and (β) in Table 1).

The single sharp preedge transition found in the $t\text{-Li}_x\text{Mn}_2\text{O}_4$ sample, which consists almost entirely of $[\text{Mn}^{3+}\text{O}_6]$ octahedra, indicates a different Mn 3d orbital arrangement as compared to the $c\text{-Li}_x\text{Mn}_2\text{O}_4$. A multiple-scattering X α calculation was performed by Kai et al.⁴⁷ for the Mn^{3+} energy levels in D_{4h} symmetry. In their calculations, the Jahn–Teller effect results in the splitting of the t_{2g} into a stabilized e_g and destabilized b_{2g} whereas the e_g splits into stabilized a_{1g} and destabilized b_{1g} states with an approximately 1 eV difference between b_{2g} and a_{1g} . Adopting this view of the electronic structure, we believe that the preedge transition at 6540.5 eV in $t\text{-Li}_x\text{Mn}_2\text{O}_4$ (feature (α) in Figure 1, right) results from transitions to both the e_g and b_{2g} levels; their separation is unresolvable, whereas transitions to the a_{1g} and b_{1g} MO levels are spread into the rising edge. Our interpretation is supported by the Mn K-edge XANES

data on $\beta\text{-MnOOH}$ in ref 12 which displays two clearly resolved preedge peaks that are shifted to lower energy with respect to various MnO_2 mineral samples. The higher energy preedge peak from $\beta\text{-MnOOH}$ was less intense than the lower energy peak whereas the preedge peaks from MnO_2 mineral samples in the same study were more intense than either $\beta\text{-MnOOH}$ preedge peak. $\beta\text{-MnOOH}$ is a distorted $[\text{Mn}^{3+}\text{O}_6]$ octahedral compound with a smaller c/a -axis ratio (approximately equal to 1.05 from the data given in ref 48) compared to the tetragonal Mn^{3+} spinels studied here. The smaller degree of tetragonal distortion leads to a lower degree of splitting among the various levels. The difference in the preedge peak energy separation for $\beta\text{-MnOOH}$ in ref 12 was approximately 2 eV. It follows that the greater preedge peak energy separation expected for the tetragonal Mn^{3+} spinels studied here should increase the second peak position to above 6543 eV making it indistinguishable from the rising edge and yielding a single observable preedge peak.

XANES Main Peak Shift. XANES main peak energies are affected when the core–electron binding energy is altered by changing the bond distance or electronic charge density on the absorbing ion.⁴⁹ Following reaction 1, the average nominal Mn oxidation state is expected to change from +3.50 to +3.90 upon delithiating LiMn_2O_4 to $\text{Li}_{0.2}\text{Mn}_2\text{O}_4$ ($\lambda\text{-MnO}_2$). This oxidation state change is 80% of that occurring upon changing the nominal Mn oxidation state from +3.50 to +3.00 as is expected upon lithiating LiMn_2O_4 to $\text{Li}_2\text{Mn}_2\text{O}_4$ or comparing LiMn_2O_4 and either model Mn^{3+} spinel, MgMn_2O_4 or ZnMn_2O_4 . Therefore, the fact that the XANES main peak (A) shift upon delithiation, 1.0 eV, is approximately 300% smaller compared to lithiation, 2.8 eV, but more closely correlates to 80% of the shift between LiMn_2O_4 and MgMn_2O_4 or ZnMn_2O_4 , 1.5 and 1.1 eV, respectively (see Figure 1 and Table 1) indicates that significant structural differences exist between $\text{Li}_2\text{Mn}_2\text{O}_4$ and the two model Mn^{3+} tetragonal spinels.

Calculations have shown that regular $[\text{Mn}^{4+}\text{O}_6]$ octahedra are more covalent than regular $[\text{Mn}^{3+}\text{O}_6]$ octahedra.⁵⁰ The consequence of the calculated increased covalency is an increased amount of electronic charge on the Mn^{4+} site; this in turn results in a lower core–electron binding energy compared to an ionic Mn^{4+} site.⁴⁹ An estimate on the amount of increase can be made from the X α calculations of ref 50; the covalency was quantified at 69% in $[\text{Mn}^{3+}\text{O}_6]$ octahedra and 74% in $[\text{Mn}^{4+}\text{O}_6]$ octahedra. However, it was noted in the paper that the Jahn–Teller distortion of $[\text{Mn}^{3+}\text{O}_6]$ octahedra, not taken into account in the calculations, would most likely lower the calculated value for $[\text{Mn}^{3+}\text{O}_6]$ octahedra. The $[\text{Mn}^{3+}\text{O}_6]$ octahedra in $\text{Li}_2\text{Mn}_2\text{O}_4$ are distorted through the Jahn–Teller effect^{2,4} and it has been shown by EXAFS that tetragonally distorted $[\text{Mn}^{3+}\text{O}_6]$ octahedra are present within the cubic LiMn_2O_4 structure.^{32,51,52} Therefore, the covalency difference between the different $[\text{MnO}_6]$ octahedra due to the change in Mn oxidation state does not account for the different shifts observed when delithiating and lithiating LiMn_2O_4 .

The L-XES data shown in Table 3 reveal that a similar degree of covalency is present at the Mn site for MgMn_2O_4 and ZnMn_2O_4 , however the main peak (A) energy in the XANES spectrum is 0.4 eV higher in the latter. Structural data from ref 29 reveal that the Mn–O distances within MgMn_2O_4 are 2.30 and 2.01 Å along the octahedral c -axis and a -axis distances, respectively. These distances yield an average Mn–O distance of 2.11 Å and a c/a -axis ratio equal to 1.14. For ZnMn_2O_4 , data from ref 28 correspond to 2.22 and 1.95 Å for the c -axis and a -axis Mn–O distances, respectively, yielding an average Mn–O distance of 2.04 Å and a c/a -axis ratio equal to 1.14.

Given that the c/a -axis ratios and relative degree of covalency for these compounds are similar, we attribute the lower XANES main peak energy observed for MgMn_2O_4 to the greater Mn–O bond distances within the $[\text{Mn}^{3+}\text{O}_6]$ octahedra in comparison to ZnMn_2O_4 . The longer bond distances stabilize the outer molecular orbitals with respect to the 1s core level leading to a lower main peak energy.⁴⁹

The average Mn–O bond distance of $\text{Li}_2\text{Mn}_2\text{O}_4$ is 2.08 Å, between that of MgMn_2O_4 and ZnMn_2O_4 . However, the L-XES data reveal that the degree of covalency within $\text{Li}_2\text{Mn}_2\text{O}_4$ is approximately 100% larger than the Mn^{3+} model spinels based upon the estimate that a 1% increase in L_α/L_β ratio corresponds to a 1.6% increase in covalency.¹⁸ Therefore, an increased degree of covalency in $\text{Li}_2\text{Mn}_2\text{O}_4$ as compared to the model Mn^{3+} spinels is likely to be the source of the greater than expected XANES peak shift occurring upon lithiation as compared to delithiation and can be elucidated through comparison of the XANES edge structure as discussed below.

Before beginning discussion of the XANES edge results it should be noted that the higher covalency of $[\text{Mn}^{4+}\text{O}_6]$ octahedra and the subsequent effect on the binding energy was not considered by Liu et al.⁵³ in their study of the LiMn_2O_4 XANES at both the Mn K and $L_{\text{II,III}}$ -edges. The authors of this study compared the peak positions of LiMn_2O_4 to the Mn^{4+} oxide MnO_2 and the Mn^{3+} oxide Mn_2O_3 to conclude that the average Mn oxidation state in LiMn_2O_4 is close to +4. This interpretation is incorrect, given the findings in refs 13 through 16, chemical analysis of LiMn_2O_4 performed in numerous studies (e.g., ref 45), electronic and magnetic properties of LiMn_2O_4 , and results presented in this paper.

XANES Edge Structure. Features γ and ϵ in the c- $\text{Li}_x\text{Mn}_2\text{O}_4$ XANES (see Figure 1) are indicative of slight curvature in the edge. In contrast, the XANES of first-row transition-metal compounds with regular octahedral symmetry possess smooth edges.^{34,35} Oxygen ions within spinels are shifted along $\langle 111 \rangle$ to accommodate the presence of tetrahedral cations, which slightly distorts the bond angles within the octahedra.⁵⁴ The magnitude of this shift is given by the difference in the oxygen positional coordinate (the spinel u parameter) from the ideal setting of $u = 0.250$ (or 0.375 depending on the crystallographic setting). In LiMn_2O_4 the u parameter is approximately 0.2625 (or 0.3875 for the other crystallographic setting)²⁶ while it increases slightly in delithiated materials.^{6,7,26,27} Amundsen et al. modeled the XANES curvature with multiple-scattering ab initio calculations of the LiMn_2O_4 XANES.^{13,14} Presumably the distortion of the octahedral sites within the lattice contributes to the multiple-scattering which in turn causes the observed features in the c- $\text{Li}_x\text{Mn}_2\text{O}_4$ XANES rising edge.

The differences in peak B upon comparing the XANES of $\text{Li}_2\text{Mn}_2\text{O}_4$ and the Mn^{3+} spinel model compounds (Figure 3) indicate that the second and/or higher coordinate shells are different in t- $\text{Li}_x\text{Mn}_2\text{O}_4$ as compared to other tetragonal spinels.^{9,11} Lithium ions insert into the 8c (or “empty” octahedral)⁵⁵ site of t- $\text{Li}_x\text{Mn}_2\text{O}_4$ and a neutron diffraction study by David et al.⁶ concluded that approximately one-half of the tetrahedral, or original Li^+ , are displaced into the 8c site. The ionic radii of tetrahedral Li^+ , Mg^{2+} , and Zn^{2+} are approximately the same (0.59, 0.57, and 0.60 Å, respectively),⁵⁶ thus the degree of Mn–O octahedral bond angle distortion due to the tetrahedral occupancy should be the same for all three of the Mn^{3+} spinels. Therefore, the difference in peak B among the t- $\text{Li}_x\text{Mn}_2\text{O}_4$ and model tetragonal Mn^{3+} spinel XANES suggests that the 6568 eV peak in the t- $\text{Li}_x\text{Mn}_2\text{O}_4$ XANES manifests from atomic displacements due to the inserted and displaced octahedral Li^+ .

These atomic displacements result in different multiple scattering paths in comparison to those taking place in the model tetragonal Mn^{3+} spinels.

XANES of transition-metal compounds with O_h symmetry possess an edge with a single, smooth maximum^{34,35} as the three 4p states are degenerate and give rise to the molecular orbital t_{1u} . Structures in the edge such as shoulders or steps occur when the t_{1u} molecular orbital is split by a lower-symmetry coordination. For the case of axially elongated octahedral coordination (D_{4h} symmetry), the p representational splitting is $t_{1u} \rightarrow a_{2u} + e_u$. The metal–ligand interaction is lowered along the unique axis as compared to the equatorial axis; this stabilizes the a_{2u} molecular orbital and destabilizes the e_u . Experimental data³⁶ and multiple-scattering calculations^{34,36} have shown, in agreement, that the absorption edge structure is dependent upon the c/a -axis ratio for the distortion. As the degree of elongation increases, a shoulder first appears in the edge and moves to lower energy as the c/a -axis ratio increases. A distinct step halfway up the edge is observed when the c/a -axis ratio reaches values of around 1.30; the step intensity matches that expected for the ratio of transitions to a single state (a_{2u}) versus that of a doubly degenerate state (e_u).^{34,36} Furthermore, when the excitation beam is polarized along the unique axis of a distorted octahedral compound, the maximum occurs at an energy corresponding to the shoulder/step feature of the nonpolarized spectra. The converse is true when the polarization vector lies within the equatorial plane at the maximum energy of the nonpolarized main peak.³⁶

The data in Table 2 show that the edge discontinuities (δ) and main peaks (A) are more separated and at lower energies in $\text{Li}_2\text{Mn}_2\text{O}_4$ compared to the tetragonal Mn^{3+} model spinels. Combining this observation with only the XANES literature cited above and the known distances of MgMn_2O_4 and ZnMn_2O_4 would lead to the conclusion that the step appearing in t- $\text{Li}_x\text{Mn}_2\text{O}_4$ manifests from a square-planar local coordination of the Mn site with a c/a -axis ratio approximately equal to 1.30 or greater. However, this conclusion conflicts with the atomic structural results of refs 2 and 5 through 7 which reveal that the Mn site symmetry and c/a -axis ratio of t- $\text{Li}_x\text{Mn}_2\text{O}_4$ is similar to MgMn_2O_4 and ZnMn_2O_4 . At this point the sensitivity of XANES to the electronic structure arising from the local symmetry must be recalled. Taking both of the diffraction-based and XAS-based views of the t- $\text{Li}_x\text{Mn}_2\text{O}_4$ structure into account suggests that the Mn coordination polyhedra in t- $\text{Li}_x\text{Mn}_2\text{O}_4$ can be described as atomically, or geometrically, tetragonal-distorted octahedra but electronically square planar. To understand this seemingly contradictory description, we must consider the differences among stoichiometry, bond nature, and site occupancy of t- $\text{Li}_x\text{Mn}_2\text{O}_4$ versus that of the tetragonal Mn^{3+} model spinels.

One consequence of the inserted “guest” ion of intercalation or insertion compounds is the polarization of the anionic “host” lattice.⁵⁷ In spinels, the occupied and empty interstitial octahedral sites of the oxygen-based lattice are coplanar. Therefore, it would be expected that the inserted, 8c Li^+ of t- $\text{Li}_x\text{Mn}_2\text{O}_4$ will polarize the oxygen within the same plane as the equatorial Mn–O bonds. The neutron-diffraction study conducted by David et al.⁶ determined that the Li^+ inserted at $x > 1$ together with displaced tetrahedral Li^+ occupy approximately three-quarters of the 8c sites in t- $\text{Li}_x\text{Mn}_2\text{O}_4$. The Pauling electronegativity difference for Mg–O and Zn–O are 2.3 and 1.9, respectively, translating to an expected ionic character of 74% and 59%, respectively. The nearly identical XES L_α/L_β ratios found for ZnMn_2O_4 and MgMn_2O_4 imply that the degrees of

covalency within the Mn–O bonds are similar in these compounds and are not affected by the type of tetrahedral cation. These facts lead us to conclude that the differences in covalency among the tetragonal Mn^{3+} model spinels and $\text{t-Li}_x\text{Mn}_2\text{O}_4$ derives from the $8c$ Li^+ within the latter. The consequence of the increased covalency, in terms of a square-planar interpretation, is the redistribution of electronic charge density away from the Mn–O bond along the unique (4-fold) axis. In other words, there is less overlap between the Mn 3d and oxygen $2p_z$ orbitals and increasing electronic charge density within the equatorial Mn–O bonds making the lithiated, tetragonal spinel somewhat analogous to a layered compound. This lowers the a_{2u} (Mn $4p_z$) level with respect to the e_u ($4p_x$ & $4p_y$) level by an amount greater than that found in tetragonal AB_2O_4 spinels possessing the same degree of octahedral distortion but empty $8c$ sites (e.g., MgMn_2O_4 and ZnMn_2O_4). The result of the increased splitting is the formation of the distinct edge step in the XANES.

The observed low energy peaks or steps found in the main edges of Cu(II) complexes have been attributed to a $1s \rightarrow 4p_z + \text{LMCT}$ shakedown transition.^{37,38} The phenomenology of this transition manifests from the relaxation of metal valence orbital levels to lower binding energy upon creation of a core-hole. An electron can then transfer to the metal from a ligand when the metal valence levels are below those of the ligand, giving rise to a feature on the rising edge.³⁸ As shown in ref 37 and explained in ref 38, an increased degree of covalency decreases the shakedown transition energy due to the greater relative stabilization of the metal valence orbital upon core ionization with respect to the ligand valence orbitals. Therefore, this interpretation of the $\text{t-Li}_x\text{Mn}_2\text{O}_4$ XANES also entails an increased degree of covalency in $\text{t-Li}_x\text{Mn}_2\text{O}_4$ as compared to nonlithiated tetragonal spinels such as MgMn_2O_4 and ZnMn_2O_4 . The fact that a similar step was found in the Mn as well as Cr XANES of $\text{t-Li}_x\text{Mn}_{2-y}\text{Cr}_y\text{O}_4$ in ref 40 indicates that the described phenomenology extends to other transition-metals residing on the $8d$ site. This has implications that are discussed within the next section.

The phenomenology of the $1s \rightarrow 4p + \text{LMCT}$ shakedown process explains how an atomically tetragonal compound can possess an XANES structure similar to an atomically square planar compound. For this study, the importance of these considerations lies in the fact that the inserted Li^+ has a remarkable effect on the electronic structure. This effect, an increased degree of covalency, has not been discerned from previous electrochemical or structural investigations on this system. The fact that covalency plays a role within the structure of lithium manganospinel is not surprising as determination of the supertransferred hyperfine field coupling constant (through magnetic susceptibility and ^7Li NMR measurements) suggested that covalency increases upon partial Mn substitution in $\text{LiMn}_{2-y}\text{Me}_y\text{O}_4$, where $\text{Me} = \text{Li}, \text{Co}, \text{or Ni}$.⁵⁸ This finding has recently been confirmed with L-XES.¹⁹

Correlation of Results to Properties and Performance.

From the first-order nature of reaction 1 the lithiation, or discharge, of a LiMn_2O_4 particle can be envisioned as a shrinking core of $\text{c-Li}_x\text{Mn}_2\text{O}_4$ with $\text{Li}_2\text{Mn}_2\text{O}_4$ comprising the periphery. Therefore, for discharge to continue Li^+ must transport through $\text{Li}_2\text{Mn}_2\text{O}_4$. It has been observed that the Li^+ diffusion constant is lower in $\text{t-Li}_x\text{Mn}_2\text{O}_4$ compared to $\text{c-Li}_x\text{Mn}_2\text{O}_4$,^{4,59,60} which translates to the poor rate capabilities of the compositional region $x > 1$ (the lower discharge plateau). An explanation for this behavior is not readily apparent when considering that the Li^+ diffusion pathway is similar for both phases (through octahedral-tetragonal-octahedral sites^{2,4}), the

unit cell volume is larger in $\text{t-Li}_x\text{Mn}_2\text{O}_4$ and vacancies for Li^+ transport exist on both octahedral and tetrahedral sites within each compositional region.⁶ Early work on the LiMn_2O_4 system⁴ proposed that the dynamic Jahn–Teller Effect (JTE) present within the $[\text{Mn}^{3+}\text{O}_6]$ octahedra in $\text{c-Li}_x\text{Mn}_2\text{O}_4$ ^{32,51,52} enhances Li^+ transport. This work proposed that the lower Li^+ transport arises from the fact that the dynamic JTE is extinguished into a static JTE within $\text{t-Li}_x\text{Mn}_2\text{O}_4$. However, our work suggests another contribution, the increased “drag” on the Li^+ arising from its above-described polarization of the oxygen ions within $\text{t-Li}_x\text{Mn}_2\text{O}_4$. The results presented in ref 40 on $\text{t-Li}_x\text{Mn}_{2-y}\text{Cr}_y\text{O}_4$ indicate that Mn substitution may not combat this contribution to the slower Li^+ transport.

An electron must accompany the inserted cation in order to maintain charge neutrality within the host. Electronic conduction in $\text{c-LiMn}_2\text{O}_4$ results from a small-polaron mechanism wherein the electron hops between the Mn^{3+} and Mn^{4+} sites.⁴⁴ However, the results presented in Figures 1 and 2 along with the results from $K\beta$ X-ray emission spectroscopy measurements in ref 52 show that the electron accompanying the insertion of a Li^+ reduces a Mn^{4+} to Mn^{3+} . It would be expected that since tetragonal spinels with 100% Mn^{3+} occupancy of the $8d$ site are insulators (e.g., Mn_3O_4 ⁶¹), lithiation of the core would be prevented once $\text{Li}_2\text{Mn}_2\text{O}_4$ formed in the periphery. Electron localization occurs when it is more energetically favorable for it to polarize an atomic site than to reside within the narrow electronic bands of the solid.⁶¹ The polarization energy is proportional to the dielectric constant whereas the band energy is proportional to the bandwidth, $W/2$. An increased degree of covalency decreases the dielectric constant but increases the bandwidth. Therefore, it can be speculated that the electronic transport changes from a small-polaron mechanism in $\text{c-Li}_x\text{Mn}_2\text{O}_4$ to a band mechanism within $\text{t-Li}_x\text{Mn}_2\text{O}_4$. This transition then maintains the electronic conductivity necessary to accompany Li^+ insertion all the way to complete reduction of the Mn^{4+} within the $\text{c-Li}_x\text{Mn}_2\text{O}_4$ core to Mn^{3+} .

As mentioned within the Introduction, the low decomposition temperature of $\text{t-Li}_x\text{Mn}_2\text{O}_4$ inhibits determination of the electronic conduction mechanism by more traditional means. However, the insight into electronic structure determined from our X-ray spectroscopy results provides an interpretation of the electronic conduction mechanism during lithiation.

Conclusions

Manganese XANES and L-XES were used to study the changes in local atomic and electronic structure occurring upon changing the Li content in $\text{Li}_x\text{Mn}_2\text{O}_4$. Comparing the XANES peak positions from LiMn_2O_4 and its chemically delithiated derivative along with the Mn^{3+} model spinels MgMn_2O_4 and ZnMn_2O_4 provides evidence supporting the assertion that Mn^{3+} is oxidized upon lithium removal. The XANES of $\lambda\text{-MnO}_2$ was similar to that of previously investigated electrochemically delithiated materials. Upon lithium insertion, the XANES peak positions indicate that Mn^{4+} is reduced. The resultant geometrically tetragonal structure has a XANES shape consistent with square-planar $[\text{MnO}_6]$ or a $1s \rightarrow 4p$ LMCT shakedown transition. The edge shape arises from an anomaly in the electronic structure attributed to the presence of Li^+ inserted into the previously empty octahedral positions within the spinel. L-XES measurements reveal that the degree of covalency is increased in $\text{Li}_2\text{Mn}_2\text{O}_4$ with respect to MgMn_2O_4 and ZnMn_2O_4 , two Mn^{3+} spinels possessing a similar degree of tetragonal distortion. We conclude that lithiation of LiMn_2O_4 not only causes the well-known cubic to tetragonal phase transition, but

also results in an increased degree of covalency with respect to the other Mn^{3+} tetragonal spinels studied. The increased covalency is a potential contributor to the lower rate capability of the Li^+ insertion reaction when $x > 1$ in $\text{Li}_x\text{Mn}_2\text{O}_4$ as observed in the literature.^{4,59,60} Additionally, given that LiMn_2O_4 conducts electrons via the small-polaron mechanism among the Mn^{4+} and Mn^{3+} sites, the band structure imparted by covalency provides an electronic transport mechanism for the 100% Mn^{3+} compound $\text{Li}_2\text{Mn}_2\text{O}_4$.

These results along with our previous study of the amorphous manganese-oxide insertion material, $\text{Li}_{1.5}\text{Na}_{0.5}\text{MnO}_{2.84}\text{I}_{0.12}$,⁶² demonstrate the usefulness of X-ray spectroscopies for characterizing the electronic structure of powders that are not amenable to study by techniques requiring sample fabrication or measurement at elevated temperatures. Direct characterization of the electronic structure can reveal the origin of physical properties that are unexplained when considering the atomic structure alone.

Acknowledgment. This work was supported by the Director, Office of Energy Research, Office of Basic Energy Sciences, Chemical Sciences Division of the U.S. Department of Energy under Contract No. DE-AC03-76SF00098 to the Ernest Orlando Lawrence Berkeley National Laboratory and the National Science Foundation, Grant No. DMR-9017996. The Stanford Synchrotron Radiation Laboratory is funded by the Department of Energy, Office of Basic Energy Sciences. The Advanced Light Source is supported by the Office of Basic Energy Science, U.S. Department of Energy Contract No. DE-AC03-76SF00098.

References and Notes

- Wickham, D. G.; Croft, W. J. *J. Phys. Chem. Solids* **1958**, 7, 351.
- Thackeray, M. M.; David, W. I. F.; Bruce, P. G.; Goodenough, J. B. *Mater. Res. Bull.* **1983**, 18, 461.
- Tarascon, J. M.; Guyomard, D. *Electrochem. Acta* **1993**, 38, 1221.
- Goodenough, J. B.; Thackeray, M. M.; David, W. I. F.; Bruce, P. G. *Rev. Chem. Miner.* **1984**, 21, 435.
- Mosbah, A.; Verbaere, A.; Tournoux, M. *Mater. Res. Bull.* **1983**, 18, 1375.
- David, W. I. F.; Thackeray, M. M.; De Picciotto, L. A.; Goodenough, J. B. *J. Solid State Chem.* **1987**, 67, 316.
- Ohzuku, T.; Kitagawa, M.; Hirai, T. *J. Electrochem. Soc.* **1990**, 137, 769.
- Glen, G. L.; Dodd, C. G. *J. Appl. Phys.* **1968**, 39, 5372.
- Belli, M.; Scafati, A.; Bianconi, A.; Mobilio, S.; Palladino, L.; Reale, A.; Burattini, E. *Solid State Comm.* **1980**, 35, 355.
- Knapp, G. S.; Veal, B. W.; Pan, H. K.; Klippert, T. *Solid State Commun.* **1982**, 44, 1343.
- Grunes, L. A. *Phys. Rev. B* **1983**, 27, 2111.
- Manceau, A.; Gorshkov, A. I.; Drits, V. A. *Am. Miner.* **1992**, 77, 1133.
- Ammundsen, B.; Jones, D. J.; Rozière, J.; Burns, G. R. *Chem. Mater.* **1996**, 8, 2799.
- Ammundsen, B.; Jones, D. J.; Rozière, J. *J. Solid State Chem.* **1998**, 141, 294.
- Shiraishi, Y.; Nakai, I.; Tsubata, T.; Himeda, T.; Nishikawa, F. *J. Solid State Chem.* **1997**, 133, 587.
- Shinshu, F.; Kaida, S.; Nagayama, M.; Nitta, Y. *J. Power Sources* **1997**, 68, 609.
- Butorin, S. M.; Galakhov, V. R.; Kurmaev, E. Z.; Glazyrina, V. I. *Solid State Commun.* **1992**, 81, 1003.
- Grush, M. M.; Muramatsu, Y.; Underwood, J. H.; Gullikson, E. M.; Ederer, D. L.; Perera, R. C. C.; Callcot, T. A. *J. Elect. Spectrosc.* **1998**, 92, 225.
- Grush, M. M.; Horne, C. R.; Perera, R. C. C.; Ederer, D. L.; Cramer, S. P.; Cairns, E. J.; Callcott, T. A. *Chem. Mater.* **2000**, 12, 659.
- Kingery, W. D.; Bowen, H. K.; Uhlmann, D. R. *Introduction to Ceramics*, 2nd ed.; J. Wiley and Sons: New York, 1976.
- Hunter, J. C. *J. Solid State Chem.* **1981**, 39, 142.
- Richardson, T. J.; Ross, P. N. *Mater. Res. Bull.* **1996**, 31, 935.
- Feldman, L. C.; Mayer, J. W. *Fundamentals of surface and thin film analysis*; North-Holland: New York, 1986.
- Tarascon, J. M.; Guyomard, D. *J. Electrochem. Soc.* **1991**, 138, 2864.
- Holland, T. B. J.; Redfern, S. A. T. *Mineralogical Mag.* **1997**, 61, 65.
- Fong, C.; Kennedy, B. J.; Elcombe, M. M. *Z. Kristallogr.* **1994**, 209, 941.
- Kanamura, K.; Naito, H.; Yao, T.; Takehara, Z. *J. Mater. Chem.* **1996**, 6, 33.
- Yanamoto, N.; Kawano, S.; Achiwa, N.; Higashi, S. *FOFUA* **1983**, 30, 48.
- Sanjana, N. R.; Biswas, A. B.; Sinha, A. P. B. *JSIIB* **1960**, 19, 415.
- Jia, J. J.; Callcot, T. A.; Yurkas, J.; Ellis, A. W.; Himpsel, F. J.; Samant, M. G.; Stohr, J.; Ederer, D. L.; Carlisle, J. A.; Hudson, E. A.; Terminello, L. J.; Shuh, D. K.; Perera, R. C. C. *Rev. Sci. Instrum.* **1995**, 66, 1394.
- Butorin, S. M.; Guo, J.-H.; Magnuson, M.; Kuiper, P.; Nordgren, B. *Phys. Rev. B* **1996**, 54, 4405.
- Cairns, E. J.; Horne, C. R.; Weiss, B. J. R.; Grush, M. M.; Cramer, S. P. In *Proceedings of the Second International Symposium on New Materials for Fuel Cell and Modern Battery Systems*; Montreal, July 1997; Savadogo, O., Roberge, P. R., Eds.; École Polytechnique de Montréal: Montréal 1997; p 336.
- Cotton, F. A.; Hanson, H. P. *J. Chem. Phys.* **1956**, 25, 619.
- Garcia, J.; Benfatto, M.; Natoli, C. R.; Bianconi, A.; Fontaine, A.; Tolentino, H. *Chem. Phys.* **1989**, 13, 2295.
- Garcia, J.; Bianconi, A.; Benfatto, M.; Natoli, C. R. *J. Phys.* **1986**, 47, C8-49.
- Palladino, L.; Della Longa, S.; Reale, A.; Belli, M.; Scafati, A.; Onori, G.; Santucci, A. *J. Chem. Phys.* **1993**, 98, 2720.
- Kau, L. S.; Spira-Solomon, D. J.; Penner-Hahn, J. E.; Hodgson, K. O.; Solomon, E. I. *J. Am. Chem. Soc.* **1987**, 109, 6433.
- Shadle, S. E.; Penner-Hahn, J. E.; Schugar, H. J.; Hedman, B.; Hodgson, K. O.; Solomon, E. I. *J. Am. Chem. Soc.* **1993**, 115, 767.
- (a) Blair, R. A.; Goddard, W. A. *Phys. Rev. B* **1980**, 22, 2767. (b) Kosugi, N.; Yokoyama, T.; Asakuna, K.; Kuroda, H. *Springer Proc. Phys.* **1984**, 2, 55. (c) Kosugi, N.; Yokoyama, T.; Asakuna, K.; Kuroda, H. *Chem. Phys.* **1984**, 91, 249.
- Ammundsen, B.; Jones, D. J.; Rozière, J.; Villain, F. *J. Phys. Chem. B* **1998**, 102, 7939.
- Hahn, J. E.; Scott, R. A.; Hodgson, K. O.; Doniach, S.; Desjardins, S. R.; Solomon, E. I. *Chem. Phys. Lett.* **1982**, 88, 595.
- International Tables for Crystallography*, 4th rev. ed; Hahn, T. Ed.; Kluwer Academic Publishers: Dordrecht, 1995.
- (a) Preudhomme, J.; Tarte, P. *Spectrochim. Acta* **1971**, 27A, 845. (b) Preudhomme, J.; Tarte, P. *Spectrochim. Acta* **1971**, 27A, 1817. (c) Lutz, H. D.; Müller, B.; Steiner, H. J. *J. Solid State Chem.* **1991**, 90, 54. (d) Allen, G. C.; Paul, M. *Appl. Spectrosc.* **1995**, 49, 451. (e) Richardson, T. J.; Wen, S. J.; Striebel, K. A.; Ross, P. N.; Cairns, E. J. *Mater. Res. Bull.* **1997**, 32, 609.
- Sheftel, I. T.; Pavlotskii, Y. V. *Inorg. Mater. (USSR)* **1966**, 2, 918.
- Masquelier, C.; Tabuchi, M.; Ado, K.; Kanno, R.; Kobayashi, Y.; Maki, Y.; Nakamura, O.; Goodenough, J. B. *J. Solid State Chem.* **1996**, 123, 255.
- Cox, P. A. *Transition Metal Oxides: An Introduction to their Electronic Structure and Properties*; Oxford University Press: Oxford, U.K., 1992.
- Kai, A. T.; Larsson, S.; Hälenius, U. *Phys. Chem. Miner.* **1980**, 6, 77.
- Garrido, J. *COREA* **1935**, 200, 69.
- Bianconi, A. XANES Spectroscopy. In *X-ray Absorption: Principles, Applications, Techniques of EXAFS, SEXAFS and XANES*; Koningsberger, D. C., Prins, R., Eds.; J. Wiley & Sons: New York, 1988; p 573.
- Sherman, D. M. *Am. Miner.* **1984**, 69, 788.
- Yamaguchi, H.; Yamada, A.; Uwe, H. *Phys. Rev. B* **1998**, 58, 8.
- Horne, C. R.; Bergmann, U.; Grush, M. M.; Weiss, B. J. R.; Cairns, E. J.; Cramer, S. P. Submitted to *Phys. Rev. B*.
- Liu, R. S.; Jang, L. Y.; Chen, J. M.; Tsai, Y. C.; Hwang, Y. D.; Liu, R. G. *J. Solid State Chem.* **1997**, 128, 126.
- Valenzuela, R. *Magnetic Ceramics*; Cambridge University Press: New York, 1994.

(55) In normal AB_2X_4 spinels the anions, usually oxygen, form a close-packed array and the B cations occupy one-half of the available octahedral sites within the array. In the $Fd\bar{3}m$ space group of cubic spinels the “empty” octahedral site is given by Wyckoff symbol 16c. In the tetragonal spinel space group $I4_1/amd$ this same position, the “empty” octahedral site, is now the 8c site given the lower symmetry of the space group and concomitant smaller unit cell.

(56) Shannon, R. D. *Acta Crystallogr.* **1976**, A32, 751.

(57) McKinnon, W. R.; Haering, R. R. In *Physical Mechanisms of Intercalation*; White, R. E., Bockris, J. O'M., Conway, B. E. Eds.; Modern Aspects of Electrochemistry Vol. 15; Plenum Press: New York, 1983; p 235.

(58) Gee, B.; Horne, C. R.; Cairns, E. J.; Reimer, J. A. *J. Phys. Chem. B* **1998**, 102, 10142.

(59) Barker, J.; Pynenburg, R.; Koksang, R. *J. Power Sources* **1994**, 52, 185.

(60) Striebel, K. S.; Rougier, A.; Horne, C. R.; Reade, R. P.; Cairns, E. *J. J. Electrochem. Soc.* **1999**, 146, 4339–4397.

(61) Cox, P. A. *The Electronic Structure of Solids*; Oxford University Press: Oxford, U.K., 1988.

(62) Horne, C. R.; Bergmann, U.; Kim, J.; Streibel, K. A.; Manthiram, A.; Cramer, S. P.; Cairns, E. J. *J. Electrochem. Soc.* **2000**, 147, 395.